

## Peak separation and small-signal modeling analysis of abnormal shift in the transconductance curve in InAs composite channel HEMT

GONG Yong-Heng<sup>1,2</sup>, CHEN Yu-Xuan<sup>1,2</sup>, SHI Jing-Yuan<sup>1</sup>, ZHANG Da-Yong<sup>1</sup>, SU Yong-Bo<sup>1</sup>,  
DING Wu-Chang<sup>3</sup>, DING Peng<sup>1,2\*</sup>, JIN Zhi<sup>1,4\*</sup>

- (1. High-Frequency High-Voltage Device and Integrated Circuits Center, Institute of Microelectronics, Chinese Academy of Sciences, Beijing 100029, China;
2. University of Chinese Academy of Sciences, Beijing 100049, China;
3. Institute of Semiconductors, Chinese Academy of Sciences, Beijing 100083, China;
4. International School of Microelectronics, Dongguan University of Technology, Dongguan 523808, China)

**Abstract:** In this work, 100 nm gate-length InP-based high electron mobility transistors (HEMTs) with a composite InGaAs/InAs/InGaAs channel are fabricated. DC measurements indicate that the InAs channel enhances transconductance but shifts the peak point toward lower  $V_{gs}$  under high  $V_{ds}$  bias. Peak separation analysis reveals the DC transconductance curve is composed of two components: the gate-controlled transconductance and the impact-ionization-induced additional transconductance. Further analysis demonstrates that the anomalous shift originates from the channel impact ionization intensity variation, which is caused by changes in the gate-drain electric field rather than the carrier density in the channel. Two additional current sources are introduced in the small-signal model to characterize the impact-ionization-induced transconductance, and the numerical variation trends of their parameters are consistent with the peak separation results, which validate the mechanism's correctness. RF measurements confirm that the DC transconductance enhancement does not effectively improve RF characteristics, which is attributed to the ionization-induced transconductance having a time constant significantly larger than that of conventional transconductance components. These findings provide a theoretical foundation for controlling the impact-ionization.

**Key words:** HEMTs, InAs, peak separation, impact ionization, transconductance, small-signal equivalent model

## 对 InAs 复合沟道 HEMT 中跨导曲线异常偏移的峰分离和小信号模型分析

巩永恒<sup>1,2</sup>, 陈宇轩<sup>1,2</sup>, 史劲元<sup>1</sup>, 张大勇<sup>1</sup>, 苏永波<sup>1</sup>, 丁武昌<sup>3</sup>, 丁芃<sup>1,2\*</sup>, 金智<sup>1,4\*</sup>

- (1. 中国科学院微电子研究所 高频高压器件与集成电路研究中心, 北京 100029;
2. 中国科学院大学, 北京 100049;
3. 中国科学院半导体研究所, 北京 100083;
4. 东莞理工大学 国际微电子学院, 广东 东莞 523808)

**摘要:** 本研究成功制备了栅长为 100 nm、具有 InGaAs/InAs/InGaAs 复合沟道的磷化铟基高电子迁移率晶体管 (InP HEMTs)。直流测试表明, InAs 沟道层的引入提升了跨导, 但导致跨导峰值点在高漏压 ( $V_{ds}$ ) 偏置下向低栅压 ( $V_{gs}$ ) 方向偏移。峰分离分析发现直流跨导曲线由两部分构成: 栅压调控的本征跨导和碰撞电离诱导的附加跨导。进一步研究表明, 该异常偏移源于沟道碰撞电离强度的变化, 这种变化主要由栅漏电场改变引起, 而非沟道载流子浓度的变化。小信号模型中引入的两个额外电流源表征碰撞电离跨导, 其数值变化趋势与峰分离结果的一致性验证了机理的正确性。射频测试证实, 尽管直流跨导有所提升, 但碰撞电离跨导的时间常数远大于一般跨导的时间常数, 器件射频特性未能得到有效改善。这些发现为抑制碰撞电离效应及提升有效跨导提供了理论基础。

Received date: 2024-12-27, revised date: 2025-03-04

收稿日期: 2024-12-27, 修回日期: 2025-03-04

Foundation items: Supported by the National Natural Science Foundation of China (62474195)

Biography: Gong Yong-Heng (1997—), male, Sichuan China, Ph. D. Research area involves InP HEMT and MMIC. E-mail: 472231075@qq.com

\*Corresponding author: E-mail: jinzhi@dgut.edu.cn, dingpeng@ime.ac.cn

关键词: 高电子迁移率晶体管; 砷化铟; 峰分离; 碰撞电离; 跨导; 小信号等效模型

中图分类号: TN385

文献标识码: A

## Introduction

The low-noise, high-frequency and high-gain performance characteristics make InP-based high electron mobility transistors (HEMTs) considered to be one of the most competitive semiconductor devices for millimeter and terahertz monolithic integrated circuits<sup>[1]</sup>. In 2007, R. Lai *et al.* reported a sub-50-nm device with a maximum oscillation frequency ( $f_{\max}$ ) exceeding 1 THz for the first time in InP-based HEMTs<sup>[2]</sup>. In 2015, X. B. Mei *et al.* implemented an amplifier operating at 1 THz using a 10 stage structure based on a 25 nm InP HEMT, with a gain of 9 dB<sup>[3]</sup>. This represents the single-chip amplifier circuit with the highest operating frequency reported so far.

Introducing InGaAs with high-In composition or InAs material into the channel has been proven to significantly improve the device performance due to its higher carrier mobility and saturation velocity. In 2018, Jo *et al.* reported an  $\text{In}_{0.8}\text{Ga}_{0.2}\text{As}$  HEMT with a maximum transconductance ( $g_{m,\max}$ ) of 3000 mS/mm, which achieved high performance of large gate length ( $L_g = 87$  nm) devices and represented the best performing device of the same size<sup>[4]</sup>. In 2021, Samouni *et al.* reported a 75-nm  $L_g$  InAs channel HEMT with a maximum transconductance of 1331 mS, achieving a cutoff frequency ( $f_T$ ) of 260 GHz and a  $f_{\max}$  of 800 GHz<sup>[5]</sup>. W. S. Park *et al.* obtained an InP-based HEMT with a gate length of 20 nm in 2022. The  $f_T$  of the device has been increased to 750 GHz, breaking the record of InP HEMT devices, and the  $f_{\max}$  has reached 1.1 THz<sup>[6]</sup>. However, the smaller band-gap also makes the device more susceptible to channel impact ionization, leading to the occurrence of kink effect. The devices reported above all exhibit the kink effect, and this phenomenon is even more remarkable in InAs/AlSb-structured HEMT devices<sup>[7]</sup>. In 2007, Chia *et al.* discovered that the transconductance increased rapidly when the drain voltage ( $V_{ds}$ )  $\geq 0.6$  V, and the peak transconductance shifted towards the smaller gate voltage ( $V_{gs}$ ) as the drain voltage increased in their InAs channel HEMTs. Finally, they obtained the results of  $f_T = 310$  GHz and  $f_{\max} = 330$  GHz under the condition of  $V_{ds} = 0.7$  V<sup>[8]</sup>. However, they lacked the mechanistic analysis of the transconductance shift, but instead focused on seeking the optimal bias point to obtain better characteristics.

In this paper, we present the DC and RF characteristics of the composite InGaAs/InAs/InGaAs channel HEMTs. DC measurements show introducing InAs to the channel significantly increases the transconductance but exhibits an abnormal “leftward shift” as reported in Ref. [8], which we attribute to the impact ionization. The measured  $S$  parameters enable us to develop a small-signal model. Results demonstrate that the time constant of the impact-ionization-induced transconductance ( $\tau_{ii}$ ) significantly exceeds that of the conventional gate-controlled

transconductance ( $\tau_{gs}$ ), indicating that impact ionization can not respond to high-frequency signals. RF characteristics further prove the high transconductance obtained in DC measurements fails to translate into the RF performance improvement.

## 1 Device fabrication

The schematic cross-section of InP-based HEMTs is shown in Fig. 1. The epitaxial layers of the devices were grown by Gas Source Molecular Beam Epitaxy (GSMBE) on 3-inch semi-insulating InP (100) substrates. From bottom to top, the layers consist of an InP substrate, a 500-nm-thick  $\text{In}_{0.52}\text{Al}_{0.48}\text{As}$  buffer layer, 10-nm-thick composite channel layer which contains a 3-nm-thick  $\text{In}_{0.53}\text{Ga}_{0.47}\text{As}$  layer, a 5-nm-thick InAs layer, and another 2-nm-thick  $\text{In}_{0.53}\text{Ga}_{0.47}\text{As}$  layer, then a 3-nm-thick  $\text{In}_{0.52}\text{Al}_{0.48}\text{As}$  spacer layer, a  $\delta$ -doping plane with a concentration of  $5 \times 10^{12} \text{ cm}^{-2}$ , 12-nm-thick  $\text{In}_{0.52}\text{Al}_{0.48}\text{As}$  barrier layer, and a Si-Doped  $\text{In}_{0.65}\text{Ga}_{0.35}\text{As}/\text{In}_{0.53}\text{Ga}_{0.47}\text{As}/\text{In}_{0.52}\text{Al}_{0.48}\text{As}$  (10/15/15 nm) composite capping layer.

The InP HEMT fabrication processes are similar to our previously reported devices<sup>[9]</sup>. The only difference is that the  $\text{SiO}_2$  hard mask on the surface of the device is not removed. The distance between the source and drain electrodes is designed as 2.4  $\mu\text{m}$ . The gate metal is in the middle of the gate recess, and the length of the T-gate is 100 nm, as shown in Fig. 2(a).

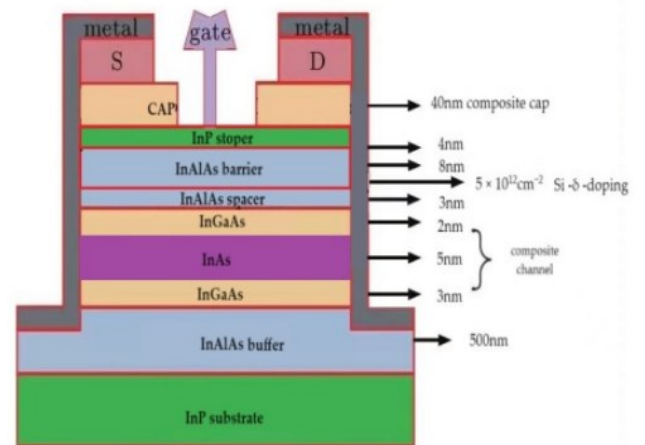
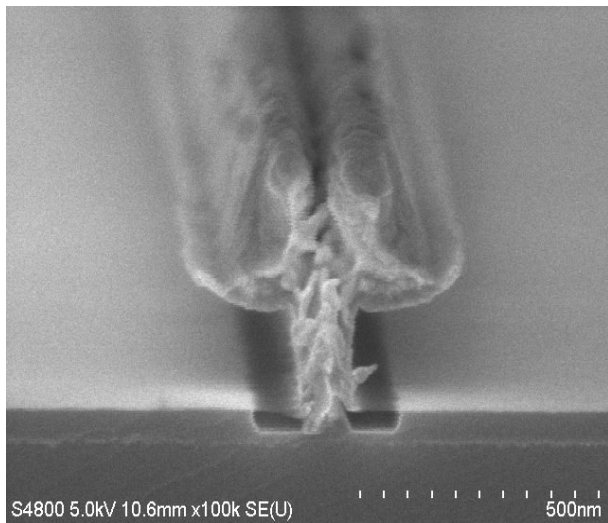


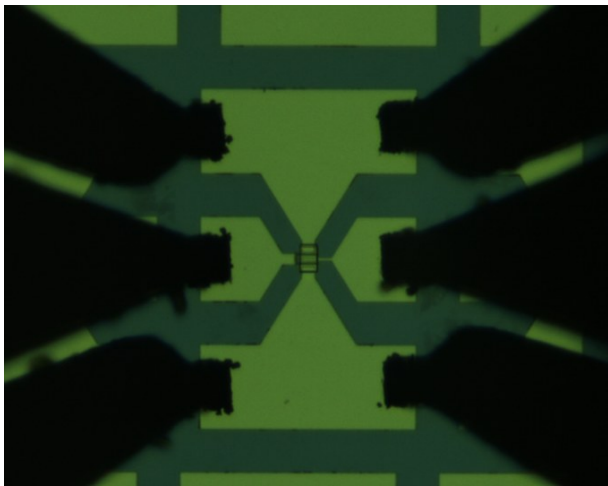
Fig. 1 Schematic cross-section of InP-based HEMTs  
图1 InP基HEMT横截面示意图

## 2 Results and discussion

The DC and RF characteristics of InGaAs/InAs/InGaAs HEMTs were characterized by HP4142 semiconductor parameter analyzer and Agilent E8363B PNA vector network analyzer from 1 to 40 GHz under room-temperature conditions, as shown in Fig. 2(b).



(a)



(b)

Fig. 2 Fabrication and testing characterization of T-shaped gate HEMT devices with 100 nm gate length: (a) SEM image of the T-Gate HEMTs, and (b) in situ electrical testing photograph of the T-gate HEMTs

图2 栅长为 100 nm 的 T 型栅 HEMT 器件制备与测试表征: (a) HEMT 器件的 T 型栅 SEM 照片及 (b) 现场测试照片

## 2.1 DC characteristics

Figure 3 shows the drain current-voltage ( $I_d$ - $V_{ds}$ ) curves of the composite channel HEMT. The device has a T-shaped gate width of  $2 \times 20 \mu\text{m}$ , and the drain current in the figure has been normalized to units of mA/mm.  $V_{gs}$  is scanned from -1.5 V to 0.2 V in steps of 0.05 V, achieving a maximum drain current density ( $I_{d_{\max}}$ ) of 925.8 mA/mm, which is achieved at  $V_{ds} = 1 \text{ V}$  and  $V_{gs} = 0.2 \text{ V}$ . (The curve family ascends from bottom to top with  $V_{gs}$  increasing from -1.5 V to 0.2 V.) In our devices, the drain current does not exhibit saturation behavior with increasing  $V_{ds}$ . When  $V_{ds}$  reaches approximately 0.6 V, the output characteristic curve demonstrates significantly enhanced upward curvature compared to lower

$V_{ds}$  bias regimes, with this slope variation being more pronounced at lower  $V_{gs}$  levels.

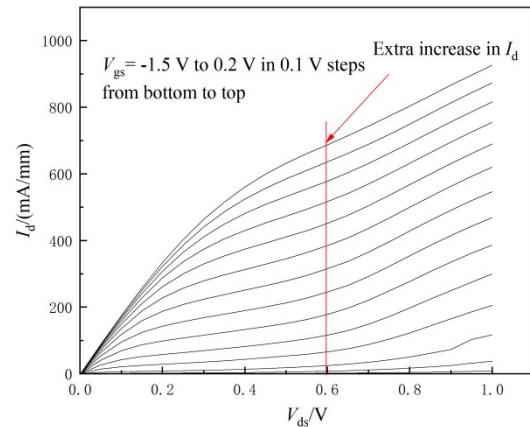


Fig. 3 Output characteristics of composite channel HEMT  
图3 复合沟道 HEMT 的输出特性曲线

When  $V_{ds}$  is high, the device operates in the saturation region where the current ideally should remain constant with further  $V_{ds}$  increase. However, the intensified electric field accelerates hot electrons to surmount the potential barrier into the buffer layer, generating additional current superimposed on the channel current. This phenomenon is quantified by the output conductance ( $g_{ds}$ ). The kink effect refers to an abrupt drain current surge occurring beyond specific  $V_{ds}$  thresholds, deviating from the predicted saturation behavior. InAs channel devices usually suffer from serious kink effect, which is generally considered to be the result of the combined effect of surface states and channel impact ionization<sup>[10]</sup>. The characteristics in Fig. 3 align with these mechanisms, where the excess  $I_d$  enhancement arises from the combined contributions of  $g_{ds}$  and kink effects.

Besides the upward curvature of the output characteristic curves, gate leakage current is more frequently employed to characterize the impact ionization. Figure 4 shows the gate leakage current versus  $V_{ds}$  from 0.5 V to 1 V with 0.1 V steps. (Curves are ordered from top to bottom with ascending  $V_{ds}$  values from 0.5 V to 1 V, where the critical point at  $V_{ds} = 0.7 \text{ V}$  is highlighted by a red line.) When  $V_{ds} \leq 0.6 \text{ V}$ , the gate leakage profile maintains consistency with conventional Schottky junction leakage behavior. Once  $V_{ds}$  reaches 0.7 V, however, the curve develops a distinct bell-shaped (or inverted U-shaped) characteristic.

The impact ionization intensity correlates with the gate-drain electric field strength. In the gate leakage current curves, as  $V_{gs}$  decreases from positive bias, the gate-drain potential difference ( $V_{dg}$ ) progressively increases. When  $V_{dg}$  exceeds the critical threshold required for impact ionization initiation, holes injected into the gate constitute additional leakage current. With further  $V_{gs}$  reduction, despite sustained strong electric fields, the two-dimensional electron gas (2DEG) in the channel becomes depleted, ceasing electron-hole pair generation through

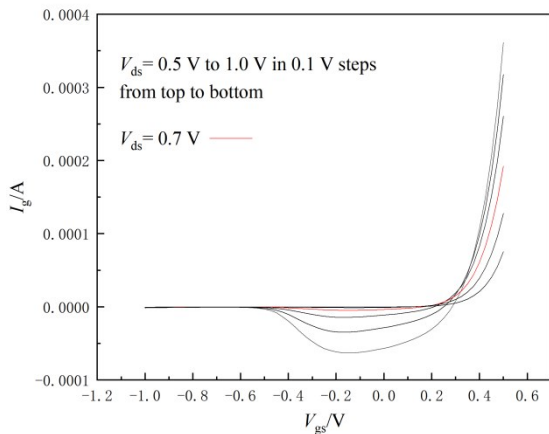


Fig. 4 The gate leakage current of the device  
图4 器件的栅极漏电流

ionization. Consequently, the gate leakage current decreases and realigns with conventional Schottky junction behavior<sup>[11]</sup>. This mechanism explains the bell-shaped profile observed in Fig. 4, confirming the impact ionization occurrence.

This analysis further elucidates the enhanced upward curvature in Fig. 3 under low  $V_{gs}$  conditions at  $V_{ds} = 0.6$  V: reduced  $V_{gs}$  elevates  $V_{dg}$ , thereby intensifying the gate-drain field and amplifying ionization effects. These observations conclusively demonstrate the impact ionization activation in high  $V_{ds}$  regimes.

Figure 5 presents the device's transfer characteristics with  $V_{gs}$  swept from -1 V to 0.5 V and  $V_{ds}$  incremented from 0 V to 1 V in 0.1 V steps. (Curves are arranged from bottom to top with  $V_{ds}$  ascending from 0 V to 1 V.) The maximum transconductance value of 1835 mS/mm is obtained at  $V_{ds} = 1$  V and  $V_{gs} = -0.3$  V. It is worth noting that the transconductance peak position exhibits  $V_{ds}$ -dependent behavior: for  $V_{ds} \geq 0.5$  V,  $V_{gs}$  corresponding to the peak transconductance no longer increases with  $V_{ds}$  as it does at low  $V_{ds}$ , but instead decreases gradually. This anomalous shift manifests as progressive leftward displacement of transconductance curve clusters under high  $V_{ds}$  conditions.

Zhong *et al.* explained the variation with bias of the transconductance curves in conventional HEMT devices in Ref. [12]: the transconductance of the device gradually increases with the increase of  $V_{ds}$ , and  $V_{gs}$  corresponding to its maximum transconductance also increases accordingly; the entire curve shows a "rightward shift" trend. This rightward displacement diminishes gradually with further  $V_{ds}$  increase and ultimately stabilizes beyond specific bias thresholds, where  $V_{gs}$  corresponding to its maximum transconductance becomes voltage-independent. Obviously, the curve clusters in Fig. 5 exhibit significant anomalies compared to those mentioned in Ref. [12].

From a functional perspective, the transconductance curve cluster can be viewed as a series of asymmetric peak functions. Under low  $V_{ds}$  bias conditions, the fitting function can characterize the asymmetry of the  $g_m$

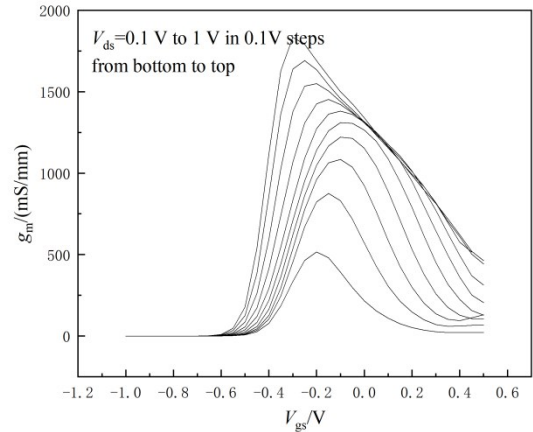


Fig. 5 The transfer characteristic curve of the device  
图5 器件的转移特性曲线

curve by using the bi-Gaussian function as:

$$y = y_0 + He^{-0.5\left(\frac{x-x_c}{w_1}\right)^2} \quad (x < x_c) \quad (1)$$

$$y = y_0 + He^{-0.5\left(\frac{x-x_c}{w_2}\right)^2} \quad (x > x_c) \quad (2)$$

However, when  $V_{ds} \geq 0.6$  V, the curve significantly deviates from a single bi-Gaussian peak shape, introducing substantial fitting residuals. The peak amplitude intensifies with concomitant leftward displacement, accompanied by measurable variations in full width at half maximum (FWHM). Although no distinct secondary peak appears in the overall curve, these features necessitate the introduction of a second peak function under high  $V_{ds}$  bias condition.

In HEMT devices, the channel current is controlled by the Schottky gate, while the impact ionization introduces parasitic current components. According to the derivative relationship between  $I_d$  and  $g_m$ , this inevitably generates parasitic transconductance contributions. Therefore, when the impact-ionization occurs, the total transconductance inherently comprises the superposition of both components; through the peak analysis of the curves, we can characterize them separately by the peak separation.

Taking the transconductance curves under the condition of  $V_{ds} = 1$  V as an example, we fit the curve with the bi-Gaussian function, and then divide it into two curves as shown in Fig. 6. The two separated curves are also characterized using Eqs. (1-2). Through this approach, we separate the transconductance curve cluster into two clusters to explain the performance of these two clusters of curves under different biases respectively, as shown in Fig. 7(a) and 7(b).

In Figs. 7 (a) and 7 (b), the transconductance curves are arranged from bottom to top in the order of progressively increasing drain-source voltage. All fitted curves exhibit determination coefficients ( $R^2$ ) exceeding 0.99, indicating a good degree of fitting. Figure 8 shows the variation of  $V_{gs}$  corresponding to  $g_{m,max}$  with  $V_{ds}$  for both transconductance components, which provides a more detailed depiction of the different shift trends shown in

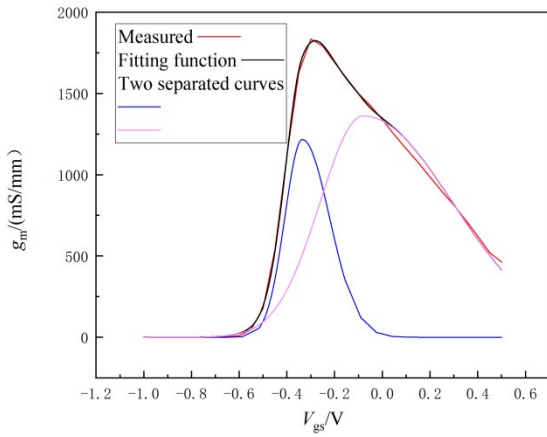


Fig. 6 The transfer characteristic curve with its fitting function curve and the two separated curves at  $V_{ds} = 1.0$  V  
图6  $V_{ds} = 1.0$  V时的转移特性曲线及其拟合曲线和两条分离曲线

Figs. 7(a) and 7(b). As shown in Fig. 7(a) and Fig. 8, when  $V_{ds} \leq 0.5$  V, there is no left shift in the measured transconductance curve, thus it can be considered that the measured  $g_m$  is well controlled by gate voltage; the trend of the entire curve cluster remains consistent with that mentioned in Ref. [12]. When  $V_{ds} \geq 0.6$  V, the impact ionization brings additional parasitic transconductance, manifesting as progressive peak left-shifting. Through peak separating, it can be inferred that the abnormal left shift of the measured transconductance curve is due to the impact ionization.

From the perspective of device physics, impact ionization intensity depends on the number of carriers entering the channel and the probability of carrier impact-ionization within the channel. The former is controlled by the gate voltage  $V_{gs}$ . Before the  $\delta$ -doped carriers fully enter the channel, it can be modeled as:

$$Q_n = Q(V_{gs}) = C_0(V_{gs} - V_{th}) \quad (3)$$

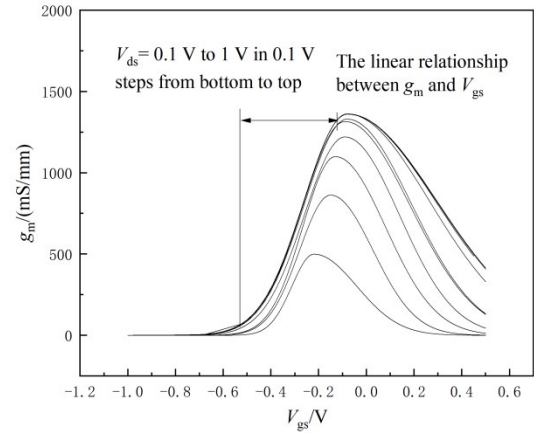
Here,  $Q_n$  denotes the gate-induced channel charge, which is capacitively coupled and characterized by capacitance  $C_0$ ;  $V_{th}$  is the threshold voltage,  $L$  is the channel length, and  $\mu_n$  is the carrier mobility. For devices operating in the saturation region, the gate controlled current and corresponding transconductance are governed by:

$$I_{dsat} = \frac{Z}{L} \int_0^L Q_n(x)v(x)dx = \frac{Z\mu_n C_0}{2L} (V_{gs} - V_{th})^2, \quad (4)$$

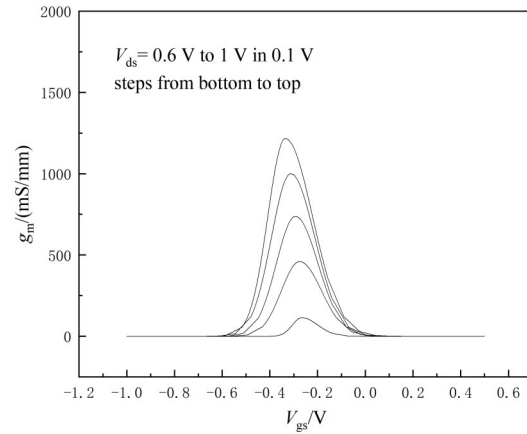
$$g_m = \frac{Z\mu_n C_0}{L} (V_{gs} - V_{th}) \quad (5)$$

At this stage,  $g_m$  and  $V_{gs}$  exhibit a linear relationship. After the  $\delta$ -doped carriers enter the channel completely,  $Q_n$  remains a constant and the channel current no longer increases with  $V_{gs}$ ,  $g_m$  progressively diminishes to 0. Figure 7(a) demonstrates that under the condition of  $V_{ds} \geq 0.6$  V, the linear  $g_m$ - $V_{gs}$  relationship persists until  $V_{gs}$  approaches -0.1 V. This also means that the linear relationship between  $Q_n$  and  $V_{gs}$  proposed in Eq. (3) has not changed.

In Fig. 7(b), the transconductance induced by the impact ionization exhibits a characteristic rise-fall profile with increasing  $V_{gs}$ , while its mechanism is similar to the



(a)



(b)

Fig. 7 Decomposition of DC transconductance curves via peak separation: (a) transconductance component controlled by the gate voltage; (b) additional transconductance component induced by the impact ionization

图7 基于峰分离法的直流跨导曲线分解结果:(a) 受到栅压调控的跨导;(b) 碰撞电离引起的额外跨导

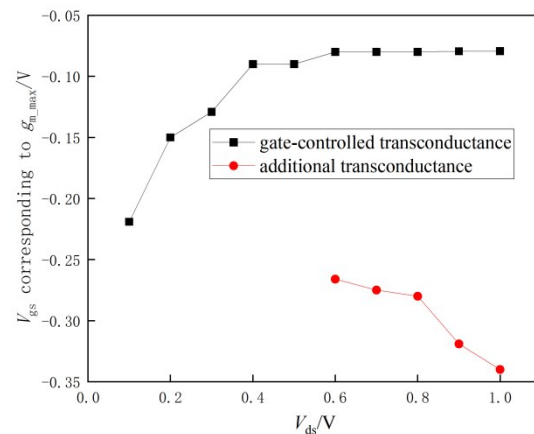


Fig. 8 Variation of  $V_{gs}$  corresponding to  $g_{m,max}$  with  $V_{ds}$   
图8 最大跨导对应的  $V_{gs}$  随  $V_{ds}$  的变化

previous explanation of bell-shaped leakage current: the initial enhancement is due to the growth of 2DEG and the decrease is due to the reduced  $V_{dg}$ . When  $V_{gs} \leq -0.1$  V,  $Q_n$  and  $V_{gs}$  maintain a linear relationship. Considering that the current generated by the impact ionization is determined by the carriers entering the channel and their ionization probabilities, therefore in Fig. 8, if ignoring the impact-ionization probability, the linear relationship between the number of carriers entering the channel and  $V_{gs}$  will make transconductance curves similar to Fig. 8 (a), and  $V_{gs}$  corresponding to peak transconductance will not change. This systematic analysis confirms that the observed peak left-shifting exclusively originates from  $V_{dg}$ -enhanced ionization probabilities. Elevated ionization efficiency reduces the required carrier density for maximum transconductance, thereby shifting the peak toward lower  $V_{gs}$  values.

### 2.2 Small-signal equivalent model

Mark Isler first introduced additional current sources in the small-signal model to account for the extra current resulting from the impact ionization in the channel. [13] On this basis, we would like to further explain the left shift phenomenon of the transconductance curve when the impact ionization occurs.

From the measured  $S$ -parameters, a small-signal equivalent model is extracted, as shown in Fig. 9. The addition of two current sources can model the impact ionization effect for large applied drain biases in the devices, which leads to an increased output conductance due to both a direct increase in the drain electron current, as well as the hole accumulation in the gate region. [14] Two current sources are controlled by  $V_{gs}$  and  $V_{dg}$  respectively, corresponding to the impact-ionization intensity affected by 2DEG and gate-drain electric field as mentioned earlier. Following the approach in Ref. [13], these effects are modeled using two frequency-dependent current sources described in Eqs. (6) and (7):

$$g_{m1} = g_{m1,ii} / (1 + j\omega\tau_{ii}) \quad , \quad (6)$$

$$g_{m2} = g_{m2,ii} / (1 + j\omega\tau_{ii}) \quad . \quad (7)$$

In Eqs. (6) and (7),  $g_{m1}$  and  $g_{m2}$  are introduced to characterize the additional transconductance generated by the impact ionization, while  $\tau_{ii}$  represents the corresponding time constant.

The influence of impact ionization is mainly restricted to low frequencies, whereas at high frequencies, impact ionization effects are not able to follow the signal. [13] The introduction of the factor  $1/(1+j\omega\tau_{ii})$  can reflect this frequency dependence. The value of  $\tau_{ii}$  is generally between 10 ps and 100 ps, which means that when the frequency exceeds 10 GHz, the real part of  $g_{m1}$  ( $g_{m2}$ ) will approach 0; when the frequency is below 1 GHz, the real part of  $g_{m1}$  ( $g_{m2}$ ) is close to  $g_{m1,ii}$  ( $g_{m2,ii}$ ).

The extraction of small-signal model parameters is based on the theory of two-port networks, starting from extrinsic elements and gradually calculating towards intrinsic elements. The extrinsic element values, which exhibit bias-independence, are extracted first and summarized in Table 1. Subsequent derivation of intrinsic admittance ( $Y$ ) parameters follows the methodology in Ref.

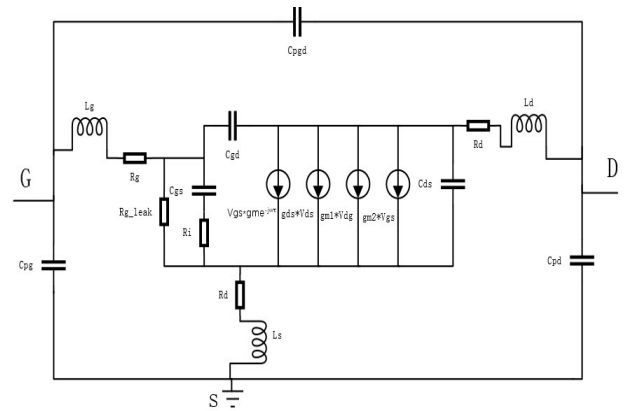


Fig. 9 Small-signal equivalent model  
图9 小信号等效模型

[15]. Here,  $L_g$ ,  $L_s$ , and  $L_d$  represent the parasitic inductances of the gate, source, and drain terminals, respectively, including contributions from metal feedlines and bonding pads. Similarly,  $R_g$ ,  $R_s$ , and  $R_d$  correspond to the parasitic resistances of these terminals, accounting for ohmic losses in the metal interconnects and pad structures. The parasitic capacitances  $C_{pd}$  (drain pad-to-ground),  $C_{pg}$  (gate pad-to-ground), and  $C_{pgd}$  (gate-to-drain pad coupling) are also quantified in this model.

Table 1 Extrinsic elements of the composite channel HEMT

表1 复合沟道HEMT器件的外部寄生参数

Extrinsic elements		
$C_{pg}=20$ fF	$L_g=40$ pH	$R_s=2$ $\Omega$
$C_{pd}=29$ fF	$L_s=4.5$ pH	$R_d=4$ $\Omega$
$C_{pgd}=9$ fF	$L_d=50$ pH	$R_g=13.8$ $\Omega$

Considering the proposed equivalent circuit model, the intrinsic  $Y$ -parameters of the HEMT are given by Eqs. (8-11):

$$Y_{11} = j\omega C_{gd} + \frac{j\omega C_{gs}}{1 + j\omega C_{gs} R_i} + \frac{1}{R_{g\_leak}} \quad , \quad (8)$$

$$Y_{12} = -j\omega C_{gd} \quad , \quad (9)$$

$$Y_{21} = -j\omega C_{gd} + \frac{g_m e^{-j\omega\tau_p}}{1 + j\omega C_{gs} R_i} + \frac{g_{m2,ii} - g_{m1,ii}}{1 + j\omega\tau_{ii}} \quad , \quad (10)$$

$$Y_{22} = j\omega(C_{gd} + C_{ds}) + g_{ds} + \frac{g_{m1,ii}}{1 + j\omega\tau_{ii}} \quad . \quad (11)$$

Intrinsic parameters have bias dependence, which can be used to study the impact of bias changes on transconductance. Here,  $C_{gs}$ ,  $C_{ds}$ , and  $C_{gd}$  represent gate-source, drain-source, and gate-drain capacitances, respectively.  $g_m$  represents the transconductance, while  $\tau_p$  is the corresponding time constant. Besides,  $R_{g\_leak}$  is introduced to characterize the gate-leakage current. Input resistance  $R_i$  governs channel charge control dynamics, while  $g_{ds}$  is the output conductance.  $C_{gd}$ ,  $C_{gs}$ ,  $R_i$ , and  $R_{g\_leak}$  can be directly extracted by decomposing the real and imaginary parts of  $Y_{11}$  and  $Y_{12}$ . And as previously

discussed, the frequency-dependent factor  $1/(1+j\omega\tau_{ii})$  allows derivation of  $g_{m1,ii}$  and  $g_{ds}$  through the following equations:

$$\text{real}(Y_{22}) = g_{ds} \quad (f > 10\text{GHz}) \quad (12)$$

$$\text{real}(Y_{22}) = g_{ds} + g_{m1,ii} \quad (f < 1\text{GHz}) \quad (13)$$

By analyzing the imaginary parts of  $Y_{21}$  and  $Y_{22}$ , substituting the value of  $g_m$ ,  $g_{ds}$ ,  $g_{m1,ii}$ , and  $g_{m2,ii}$ , calculating and tuning the system of equations at multiple frequency points, the values of  $C_{ds}$ ,  $\tau_{gs}$  and  $\tau_{ii}$  can be derived.

Figures 10 (a) and 10 (b) show the changes in  $g_{m1,ii}$  and  $g_{m2,ii}$  caused by the bias variation, respectively.  $g_{m1}$  and  $g_{m2}$  exhibit the same trend as DC characteristics: as  $V_{ds}$  gradually increases,  $V_{gs}$  corresponding to the maximum values of  $g_{m1}$  and  $g_{m2}$  gradually decreases.

Figure 11 shows the variation of maximum  $g_m$  and corresponding  $V_{gs}$  with  $V_{ds}$  in the small-signal equivalent

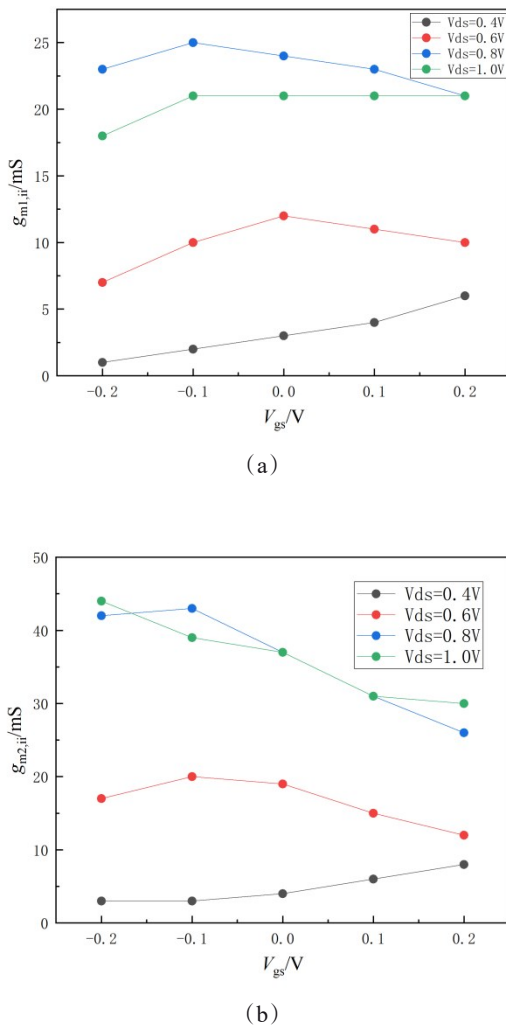


Fig. 10 Bias-dependent parameters of impact ionization-induced dual current sources in small-signal model: (a)  $g_{m1,ii}$  versus  $V_{gs}$  under different  $V_{ds}$ ; (b)  $g_{m2,ii}$  versus  $V_{gs}$  under different  $V_{ds}$ .  
图 10 小信号模型中由碰撞电离诱导的双电流源参数的偏置依赖性分析: (a)  $g_{m1,ii}$  在不同  $V_{ds}$  条件下随  $V_{gs}$  的变化; (b)  $g_{m2,ii}$  在不同  $V_{ds}$  条件下随  $V_{gs}$  的变化

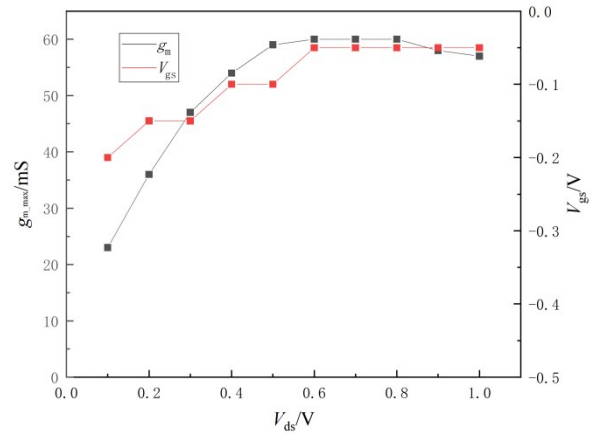


Fig. 11 The variation of  $g_{m,max}$  and corresponding  $V_{gs}$  with  $V_{ds}$ .  
图 11 最大跨导及其对应  $V_{gs}$  随  $V_{ds}$  的变化

model, and its characteristics are consistent with the results of Fig. 7 (a) and Fig. 8:  $g_{m,max}$  increases gradually with  $V_{ds}$  and approaches saturation when  $V_{ds} \geq 0.6\text{V}$ ;  $V_{gs}$  corresponding to the maximum transconductance also gradually increases and stabilizes at high  $V_{ds}$  bias. Results illustrate that the small-signal model parameters are consistent with the peak splitting results: the left shift of the transconductance curve in DC measurement is caused by the impact ionization, and the actual transconductance controlled by the gate remains consistent with the curve of a conventional HEMT device.

An exception is observed in the results of Fig. 10: at  $V_{ds} = 0.8\text{V}$ , the values of  $g_{m2,ii}$  do not consistently exceed those at  $V_{ds} = 1.0\text{V}$ , a phenomenon also reported in Ref. [13]. Nevertheless, these results still align with the physical mechanism of transconductance peak splitting observed in DC transfer characteristics- $V_{gs}$  corresponding to the maximum ionization-induced transconductance shifts leftward as  $V_{ds}$  increases. Additionally, the  $V_{gs}$  scanning step size of  $0.1\text{V}$  during testing confined the identified peak  $g_m$  values to integer grid points. This explains why Fig. 10(b) superficially suggests identical peak  $V_{gs}$  positions ( $-0.1\text{V}$ ) for both  $V_{ds} = 0.6\text{V}$  and  $0.8\text{V}$ . Furthermore, while extrinsic parasitic parameters (e. g.,  $R_s$ ,  $R_d$ ) are assumed bias-independent in the small-signal modeling, actual parasitic resistances exhibit weak bias dependence. From a device physics perspective, bias variations alter ohmic contact properties and Schottky barrier resistance, introducing systematic errors in parameter extraction<sup>[11]</sup>. These factors collectively contribute to residual discrepancies in experimental results.

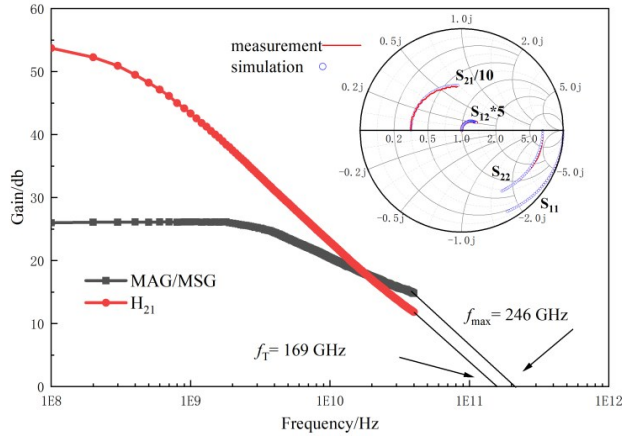
### 2.3 RF characteristics

Table 2 shows the intrinsic parameters and frequency characteristics of the device when biased at  $V_{gs} = -0.3\text{V}$  and  $V_{ds} = 1\text{V}$ . The curve of  $U_g$  often exhibits fluctuations, which can easily cause significant errors when extrapolating  $f_{max}$ . To ensure accuracy,  $f_{max}$  and  $f_{tr}$  are derived from the linear extrapolation of maximum available gain (MAG) and maximum stable gain (MSG) curves, as shown in Fig. 12.

A good fitting result of our small-signal model com-

**Table 2 Intrinsic parameters and RF characteristics of the composite channel HEMT****表2 复合沟道 HEMT 器件的本征参数和射频特性**

$C_{gs}$ (fF)	$C_{gd}$ (fF)	$C_{ds}$ (fF)	$g_{ds}$ (mS)	$g_m$ (mS)	$g_{m2,ii}$ (mS)
27	5.5	3.5	3	50	35
$g_{m1,ii}$ (mS)	$\tau_{ii}$ (ps)	$\tau_{gs}$ (ps)	$f_T$ (GHz)	$f_{max}$ (GHz)	$Ri$ ( $\Omega$ )
15	34	<1	169	246	5

Fig. 12 Extrapolation of  $f_T$  and  $f_{max}$  from measured data and the fitting result of small-signal model compared with the measured S parameters图12 测试结果外推得到的  $f_T$  和  $f_{max}$  及小信号模型 S 参数拟合

pared with the measured data is also shown in Fig. 12, which indicates the effectiveness and accuracy of our extracted parameters.

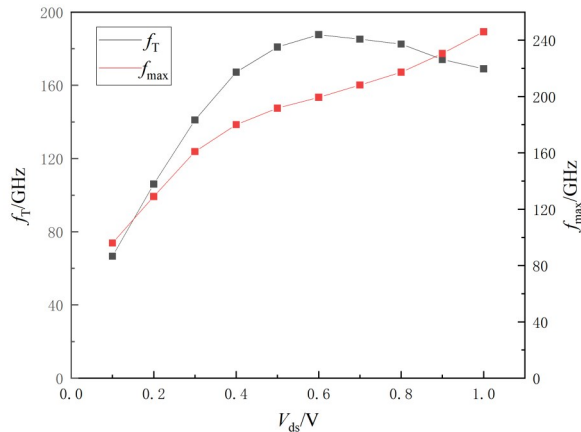
Fig. 13 RF characteristics at different  $V_{ds}$  biases  
图13 射频特性随不同  $V_{ds}$  偏置的变化

Figure 13 shows the changes in RF characteristics of the device when  $V_{ds}$  is increased from 0.1 V to 1 V with a step size of 0.1 V. The variation of  $f_T$  with  $V_{ds}$  is consistent with the trend of  $g_m$  with  $V_{ds}$  in Fig. 11, while  $f_{max}$  continues to rise with the increase of  $V_{ds}$ . The delay factor parameters in the small-signal model in Table 2 display  $\tau_{ii} \gg \tau_{gs}$ , which indicates that impact-ionization effects are not able to follow the high frequency signal.

In conventional InP-based HEMTs, the relationship between  $g_m$  and RF performance is shown in Eqs. (16) and (17)<sup>[16]</sup>:

$$f_T = \frac{g_m}{2\pi(C_{gs} + C_{gd})[1 + g_{ds}(R_s + R_d)] + C_{gd} * g_m (R_s + R_d)} \quad (16)$$

$$f_{max} = \frac{f_T}{\sqrt{4g_{ds}(R_g + R_i + R_s)} + 2C_{gd}[C_{gd}/C_{gs} + g_m(R_i + R_s)]/C_{gs}} \quad (17)$$

Based on the results of Figs. 11 and 12 with the positive correlation between  $f_T$  and  $g_m$  shown in Eq. (16), it is demonstrated that the actual gate-controlled  $g_m$  directly determines the RF characteristics. The continuous increase of  $f_{max}$  with  $V_{ds}$  is explained by Eq. (17): under high  $V_{ds}$  conditions, the output conductance  $g_{ds}$  decreases, thereby enhancing  $f_{max}$ .

The RF characteristics of this device are not as good as expected and are lower than some reported devices in Refs. [4-6]. On the one hand, the results obtained by extrapolating  $f_{max}$  from MAG/MSG are relatively conservative. On the other hand,  $\tau_{gs} \ll \tau_{ii}$ , then as mentioned earlier, the value of  $g_m$  should be corrected to the actual gate-controlled  $g_m$  to eliminate the impact of impact ionization in our devices. This significantly reduces the RF performance of the device.

Table 3 shows some key performance parameters and fabrication strategies in some recently reported InP-based HEMTs.

$g_m$  obtained by DC measurement can no longer intuitively reflect the RF characteristics, which brings greater difficulty and workload to the design and optimization of InAs channel HEMT devices. In order to control the strength of impact ionization, a gate offset in gate recess is an effective method that has been reported<sup>[11]</sup>. A gate closer to the source will increase the gate-drain distance, thereby reducing the actual gate-drain electric field to reduce the probability of carrier impact-ionization in the channel.

Compared to devices in Refs. [6] and [17], our device has a much longer  $L_g$  of 100 nm, and reducing the gate length can significantly improve  $g_m$ .

Consistent with the devices reported in Table 3, our design incorporates an InP etch-stop layer. However, this approach inadvertently increases the gate-to-channel distance (15 nm in our device vs. 9 nm in Ref. [5]), thereby degrading the gate control efficiency. Reducing this distance to < 10 nm can enhance the transconductance.

Reference [5] further highlights two common fabrication strategies for performance enhancement: asymmetric gate recess and double-side delta doping. These techniques modify key parasitic parameters (like  $C_{gd}$ ) in the small-signal model, thereby improving the RF performance. References [6] and [18] report that increasing the length of gate recess leads to changes in parasitic capacitance and resistance, thereby resulting in lower  $f_T$  and higher  $f_{max}$ . However, a larger gate recess length of-

ten leads to an increase in surface states, and the kink effect will be more pronounced, especially for our device which retains the SiO<sub>2</sub> hard mask without passivation on the gate recess surface. Therefore, implementing such fabrication strategies requires careful consideration.

Reference [9] focuses on devices with SiO<sub>2</sub> hard masks similar to ours, analyzing the impact of hard mask removal on device performance. The study concludes that removing the hard mask enhances  $f_T$  but degrades  $f_{max}$ , suggesting that hard mask retention should be application-dependent.

As discussed in Ref. [17], adjusting the InAs layer thickness within the composite channel can enhance device performance. For our 10 nm composite-channel devices, the InAs layer thickness has already reached 5 nm, which is consistent with the maximum thickness reported in Ref. [18]. Therefore, the optimization priority for our device performance focuses on the above fabrication strategies.

**Table 3 Performance parameters and fabrication strategies of InP-based HEMTs in recent literature**  
表3 近期文献中InP基HEMT器件的性能参数与制备策略

REF	$L_g/nm$	Channel	$g_{m,max}/(mS/mm)$	$f_T^I/GHz$	$f_{max}^I/GHz$	Features
[1]	100	In <sub>0.53</sub> Ga <sub>0.47</sub> As	1 120	167	1 096	Gate offset
[4]	87	In <sub>0.8</sub> Ga <sub>0.2</sub> As	3 000	559	671	\
						Asymmetric gate recess
						9 nm distance between the gate and channel
[5]	75	InAs	1 331	260	800	Double-side-doped structure
[6]	20	In <sub>0.8</sub> Ga <sub>0.2</sub> As	3 660	750	1 100	$L_{side}$ variation
[9]	80	In <sub>0.53</sub> Ga <sub>0.47</sub> As	1 087	304	524	SiO <sub>2</sub> hardmask etched
[18]	50	InAs	2 100	392	678	InAs channel inset variation

### 3 Conclusion

In summary, we have fabricated a composite InGaAs/InAs/InGaAs channel HEMT and measured its DC and RF characteristics. The transconductance curve of the device exhibits a "left shift" anomaly. Through peak separation of the transconductance curves and analysis of the small-signal equivalent model, it is determined that this phenomenon is caused by the impact ionization, resulting in additional transconductance which is not gate-controlled. This part of the transconductance has a "left

shift" trend, and this shift is mainly due to changes in the electric field strength caused by changes in  $V_{dg}$ . The RF characteristics of the device further indicate that the additional transconductance caused by the impact ionization cannot lead to higher  $f_T$  and  $f_{max}$ . Therefore, for InAs-channel devices prone to the kink effect, the RF performance degradation should be mitigated by suppressing the impact ionization, combined with a more accurate small-signal model to optimize the device design.

### References

- [1] Cao S R, Feng R Z, Wang B, et al. Impact of gate offset in gate recess on DC and RF performance of InAlAs/InGaAs InP-based HEMTs[J]. Chinese Physics B, 2022, 31(5): 827–831.
- [2] Lai R, Mei X B, Deal W R, et al. Sub 50 nm InP HEMT device with  $f_{max}$  greater than 1 THz [C]. IEEE International Electron Devices Meeting, IEEE, 2008: 609–611.
- [3] Mei X, Yoshida W, Lange M, et al. First demonstration of amplification at 1 THz using 25-nm InP high electron mobility transistor process[J]. IEEE Electron Device Letters, 2015, 36(4): 327–329.
- [4] Jo H B, Baek J M, Yun D Y, et al.  $L_g = 87$  nm InAlAs/InGaAs high-electron mobility transistors with a  $g_{m,max}$  of 3 S/mm and  $f_T$  of 559 GHz [J]. IEEE Electron Device Letters, 2018, 39(11): 1640–1643.
- [5] Samnoui M, Wichmann N, Wallart X, et al. 75 nm gate length PHEMT with  $f_{max} = 800$  GHz using asymmetric gate recess: RF and noise investigation [J]. Institute of Electrical and Electronics Engineers (IEEE), 2021, 68(9): 4289–4295.
- [6] Park W, Jo H B, Kim H J, et al. Sub-50 nm terahertz In<sub>0.8</sub>Ga<sub>0.2</sub>As quantum-well high-electron-mobility transistors for 6G applications [J]. IEEE Transactions on Electron Devices, 2023, 70: 2081–2089.
- [7] Bolognesi C R. Antimonide-based high-speed electronics: A transistor perspective[J]. IEEE, 2002: 55–58.
- [8] Chang C Y, Hsu H T, Chang E Y, et al. Investigation of impact ionization in InAs-channel HEMT for high-speed and low-power applications[J]. Electron Device Letters, IEEE, 2007, 28(10): 3.
- [9] Zhou F G, Feng R Z, Cao S R, et al. Impact of SiO<sub>2</sub> hardmask on the DC and RF characteristics of InP HEMTs[J]. Journal of Materials Science: Materials in Electronics, 2023, 34: 2005.
- [10] Rodilla H, Schlee J, Nilsson P, et al. Cryogenic kink effect in InP pHEMTs: a pulsed measurements study [J]. IEEE Transactions on Electron Devices, 2015, 62(2): 532–537.
- [11] Cao S R. Research on gate recess structure of terahertz InP HEMT for TMIC applications[D]. University of Chinese Academy of Sciences, Beijing, 2023.
- [12] Zhong Y H. Research on InP-based HEMT devices and millimeter wave monolithic amplifier circuits [D]. Xidian University, Xian, 2013.
- [13] Isler M, Schunemann K. Impact-ionization effects on the high-frequency behavior of HFETs[J]. IEEE Transactions on Microwave Theory & Techniques, 2004, 52(3): 858–863.
- [14] Johansson S, Egard M, Ghalamestani S G, et al. RF characterization of vertical InAs nanowire wrap-gate transistors integrated on Si substrates [J]. IEEE Transactions on Microwave Theory & Techniques, 2011, 59(10): 2733–2738.
- [15] Dambrine G, Cappy A, Heliodore F, et al. A new method for determining the FET small-signal equivalent circuit [J]. IEEE Transactions on Microwave Theory & Techniques, 2002, 36(7): 1151–1159.
- [16] Tasker P J, Hughes B. Importance of source and drain resistance to the maximum  $f_T$  of millimeter-wave MODFETs [J]. IEEE Electron Device Letters, 1989, 10(7): 291–293.
- [17] Feng R Z, Wang B, Cao S R, et al. Impact of symmetric gate-recess length on the DC and RF characteristics of InP HEMTs [J]. Chinese Physics B, 2022, 31(1): 788–792.
- [18] Ruiz D C, Saranovac T, Han D, et al. InAs channel inset effects on the DC, RF, and noise properties of InP pHEMTs [J]. IEEE Transactions on Electron Devices, 2019, 66(11): 4685–4691.

